A Ubiquitous GNSS-R Methodology to Estimate Surface Reflectivity Using Spinning Smartphone Onboard a Small UAS

Md Mehedi Farhad, *Student Member, IEEE*, Mehmet Kurum, *Senior Member, IEEE*, and Ali Cafer Gurbuz, *Senior Member, IEEE*

***Abstract*—Global Navigation Satellite Systems (GNSS) Reflectometry (GNSS-R) has gained significant attention in retrieving geophysical parameters of the Earth's surface using ground, airborne, and spaceborne systems in the past decade. Such studies have mainly been investigated through custom-built systems or networks of geodetic receivers and antennas. For the broader adaptation of such an approach in precision agriculture or small-scale experiments, we have recently conjectured that a smartphone's built-in GNSS chip and antenna mounted on a small Unmanned Aircraft System (UAS) platform could be used to estimate the reflectivity of the soil surface using reflected GNSS signals. The main barrier to using a smartphone as a ubiquitous GNSS-R receiver is the built-in antenna's irregular radiation pattern that makes the measurement signal highly angular dependent. This study provides a unique and practical solution to lessen the impact of antenna radiation patterns on reflectivity estimation by spinning two smartphones mounted on two separate ground plate and taking the logarithmic difference of such simultaneous measurements. In this proposed configuration, a down-facing spinning smartphone on a UAS platform collects reflected signals. At the same time, another identical spinning smartphone is located on the ground, providing reference data in an open area. We compared the results from measurements with the spinning smartphone on a small UAS and the ground. We also discuss the trade-offs involved in rotation and flight dynamics. Our findings show that a ubiquitous GNSS-R system based on spinning smartphones operating from a small UAS platform can estimate surface reflectivity at the sub-field scale.**

***Index Terms*—Global navigation satellite system reflectometry (GNSS-R), precision agriculture, reflectivity, reflectometry, smartphone, soil moisture, spinning, unmanned aircraft system (UAS).**

I. Introduction

SOIL moisture (SM) is one of the essential physical parameters of the soil. Accurate SM measurement greatly impacts agriculture production, hydrological modeling, forestry, horticulture, waste management, and other environmental fields [1]. Precision agriculture or smart farming requires high-resolution SM information to use irrigation water and other natural resources efficiently [2]. Electrical resistivity imaging, time domain reflectometry [3], frequency domain reflectometry [4], [5], [6], neutron probe [7] use a variety of implantable SM probes to retrieve subfield-scale SM at different depths. In addition, commercial three-level hygrometer sensors and monitoring other atmospheric parameters utilizing the Internet of Things (IoT) show the promising fusion of internet communication and precision agriculture [8], [9]. A prototype of a fiber optic SM probe composed of a nanoporous ceramic disk has also been developed and demonstrated its potential for large-scale deployment in precision agriculture to measure volumetric water content accurately [10]. Although SM monitoring with a low-cost wireless sensor network has been tested in the field scale, this technique also requires implanting the sensor modules into the soil, which provides point measurements [11]. The acquisition of high-resolution SM information through the utilization of various SM probes has also exhibited high accuracy and usability in the context of precision agriculture. Nonetheless, this approach demands human resources, time, and financial expenditures.

Various remote sensing methodologies have been developed to estimate SM using ground, airborne, and spaceborne microwave instruments. For instance, geodetic quality global positioning system (GPS) station that receives continuous global navigation satellite systems (GNSS) data originally used for precise positioning applications shows its potential as an SM sensor network [12]. EarthScope Plate Boundary Observatory (PBO), a stationary GPS receiver's network, provides continuous GPS data. Larson et al. [13] used this data product to monitor the SM and found a correlation of GPS signal-to-noise-ratio (SNR) with the rainfall event around the PBO sites. Furthermore, spaceborne remote sensing satellite missions utilizing the GNSS Reflectometry (GNSS-R) technique to retrieve geophysical parameters of the Earth's surface have gained significant attention in the scientific community over the last decade. The United Kingdom (U.K.)'s GNSS-R satellite mission, called TechDemoSat (TDS-1), launched in 2014 and produced numerous data products that have been used for remote sensing studies before its retirement in 2018 [14], [15], [16]. National Aeronautics and Space Administration (NASA) launched eight Low Earth Orbit (LEO) satellites on December 2016 named Cyclone Global Navigation

Manuscript received 9 May 2023; revised 20 June 2023; accepted 4 July 2023. Date of publication 12 July 2023; date of current version 24 July 2023. This work was supported by National Science Foundation under Grant 2142218. *(Corresponding author: Md Mehedi Farhad.)*

The authors are with the Department of Electrical and Computer Engineering, and Information Processing and Sensing Lab, Mississippi State University, Mississippi State, MS 39672 USA (e-mail: mf1413@msstate.edu; kurum@ece.msstate.edu; gurbuz@ece.msstate.edu).

Digital Object Identifier 10.1109/JSTARS.2023.3294833

Satellite Systems (CYGNSS) for the tracking of cyclone formation and wind direction changes using GNSS-R technique in the oceanic areas [17]. However, CYGNSS satellites also pass over the land on the Earth's surface. Many research groups worldwide took that opportunity to retrieve the volumetric SM of the land surface at 9 km to 36 km resolution using CYGNSS data product and deep learning techniques [18].

There also exists dedicated passive microwave satellite missions, such as NASA'S Soil Moisture Active Passive (SMAP) [19]. European Space Agency's Soil Moisture and Ocean Salinity (SMOS) [20] for global SM estimation with an L-band radiometer instrument that provides a spatial resolution of 36 km and temporal resolution of 1–3 days. All the existing remote sensing satellite missions for SM estimation produce numerous data products that serve many large-scale weather and climate studies and global hydrological cycle studies with their coarse spatiotemporal resolution; however, these data product does not become so useful for precision agriculture applications as they demand subfield scale high-resolution information of the geophysical parameters of the soil.

Low-cost, lightweight RF receivers, coupled with the widespread availability and advances in drones, leads to the possibility of implementing microwave remote sensing technology, originally demonstrated from space, via small unmanned aircraft system (UAS)-based platforms for high-resolution land remote sensing applications [21]. A low-cost sensor platform is developed for GNSS-R application using commercial off-the-shelf instruments and attached to a fixed-wing UAS to classify the land based on its water content. This prototype used left hand circular polarized (LHCP) and right hand circular polarized (RHCP) antennas to receive ground-reflected signals and RHCP antenna for direct line of sight signals. The offline data analysis showed clear identification of land water boundaries [22], [23]. This same GNSS-R instrument attached with a multirotor UAS showed high accuracy in detecting the water body and monitoring flooded areas with around 10-m ground resolution in [24] and [25]. A dual-polarized GNSS-R system has been developed for altimeter and detecting different surface conditions operating from a multirotor UAS. This system used the RHCP antenna and interference to perform the altimeter measurement and the LHCP antenna for the water, land, and vegetated area detection [26]. A GNSS-R polarimetric measurement platform has been developed to sense surface SM and vegetation [27]. This system consists of a dual-polarized antenna (LHCP and RHCP) to receive the ground-reflected signal and one RHCP antenna for the direct signal. They found that the polarimetric ratio is highly sensitive to the surface water content and independent of surface roughness. Single channel GNSS-R receiver attached to a small aircraft using LHCP antenna for reflected signal and RHCP antenna for the direct signal has been investigated to detect water body [28]. They used the delay difference between the direct and reflected signal to isolate the signals and used 20 ms integration time. Most recently, Senyurek et al. [29] investigated reflected GNSS signal captured via the UAS-based GNSS receivers. They developed a machine learning model with about two years of data to analyze the change of carrier to noise density ratio (CN_0) power due to the change of moisture content of the surface soil with a resolution of 5 m $\times$ 5 m. One of the main advantages of the UAS-based GNSS-R technique is that it can be implemented by using a low-cost off-the-shelf GNSS receiver and a small UAS to measure high-resolution surface reflectivity [21].

The feasibility of the smartphone's inbuilt GNSS chip and antenna for the use of the GNSS-R technique has been tested and its performance analyzed in [30]. The smartphone has been used to receive the ground-reflected GNSS signals to sense water in the soil and demonstrated that the smartphone-based GNSS receivers give the opportunity of using the existing instrument and building a low-cost sensing system that the farmers can use [31]. However, it has been observed that the smartphone's inbuilt antenna's radiation pattern is not uniform and affects the ground-reflected GNSS signals. There are nulls in the antenna radiation pattern that downgrade the received signal. Along with that, the smartphone's antenna is highly angle and orientation dependent but time-invariant.

To eliminate the smartphone's antenna's irregularity in the radiation pattern, a unique spinning mechanism has been proposed with a hypothesis that spinning the smartphone over a full rotation averages the antenna pattern and makes the acquired signal immune to the antenna pattern variations (dips/nulls) within typical orientation changes that a UAS experiences [32]. In this study, we demonstrate a direct comparison of the spinning receiver with various rotations per minute (r/min) and the nonspinning receiver placed on the ground and the impact of different spinning rates on the radiation pattern. Next, a custom quadframe UAS has been developed in the lab to test the spinning receiver system to receive the ground-reflected signal and analyze the signal quality.

The main objective of this study is to develop a UAS-based ubiquitous GNSS-R system that can retrieve high-resolution surface reflectivity for land remote sensing applications. This work utilized the reflected L-band GNSS signals to estimate the surface reflectivity in the top 5 cm of the surface soil. In contrast, most of the remote sensing approach in precision agriculture utilizes an aerial imaging-based system.

The rest of the article is organized as follows. Section II describes the general hypothesis of this work, the challenges with the instruments, and the solution to overcome the challenges, Section III presents the hardware preparation for the experiment, experimental setup, data collection process and the data preparation for analysis. Section IV provides the experimental data analysis and evaluates the results. Section V discusses tradeoffs involved in this methodology and potential applications. Finally, Section VI concludes this article.

II. Methodology

A. Concept

Our overarching research question is if we can leverage the GNSS chipset of mass-market devices, such as smartphones, on a small UAS, to apply GNSS-R methodologies for land remote sensing. In our previous work [31], we demonstrated the possibilities, but the poor quality of the built-in GNSS antennas radiation pattern was shown to be the main pitfall to achieving such a goal [30]. To lessen the impact of the antenna

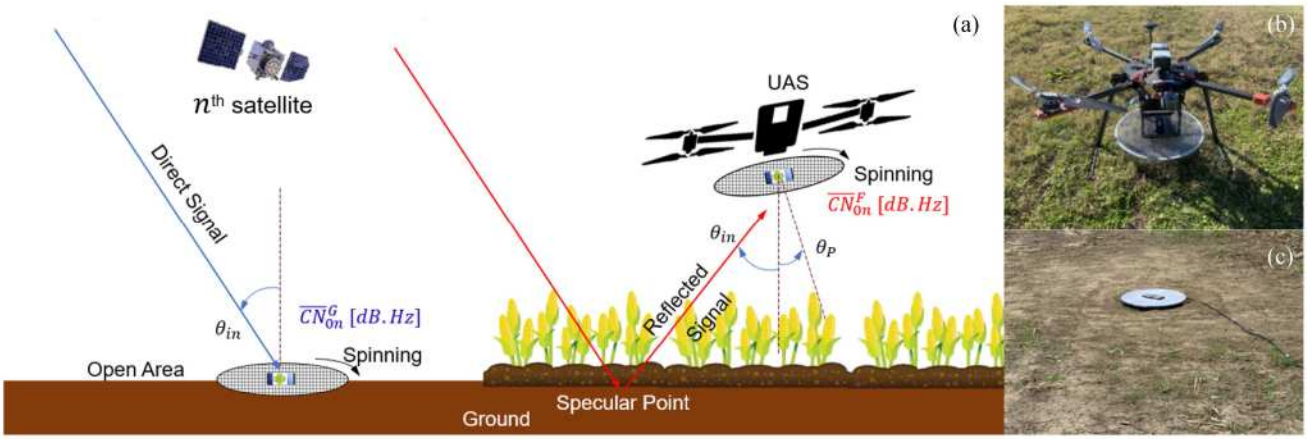

Fig. 1. (a) Simplified structure of the proposed approach is depicted where the ground unit is level and faced up straight to acquire the reference signal while the UAS unit collects the reflected signal. Reflection is assumed to be specular. Pictures of the UAS and ground setup are shown in (b) and (c), respectively.

radiation pattern irregularities on the measurement and estimate the reflectivity, we devised a unique and practical approach as illustrated in Fig. 1 [32].

The measurement concept involves a UAS equipped with a down-facing smartphone on the bottom of the UAS frame only receiving ground-reflected GNSS signal and a separate phone facing upward and placed on the ground that provides reference GNSS data in an open area. Both phones spin with a constant rotation speed to average the antenna radiation pattern. The smartphone on the UAS is placed underneath a circular mesh ground plate to isolate direct and reflected signals. We hypothesize that spinning the smartphones over a full rotation averages the antenna radiation pattern. It makes the acquired signal immune to the antenna pattern variations (dips/nulls) within typical orientation changes that UAS experiences. In fact, the idea of mechanically rotating antennas has been previously used for side lobe suppression of array antennas [33].

In this configuration, the direct (reference) GNSS signal (dB.Hz) received by the ground unit (that faces up straight) can be written as

$$\overline{CN}^{G}_{0,n} = K_n \overline{G}_R(\theta_{i,n}) \tag{1}$$

where $\overline{G}_R(\theta_{i,n})$ is the average antenna gain in the direction of incidence angle $\theta_{i,n}$ for the satellite n. The bar over the symbols represents the averaging via rotation. The constant K_n is given by

$$\mathrm{K}_n = \frac{\mathrm{P}_{T,n}\mathrm{G}_{T,n}}{4\pi \mathrm{R}_n^2}\left(\frac{\lambda^2}{4\pi}\right) \tag{2}$$

where $P_{T,n}$ and $G_{T,n}$ are the transmitted signal power and gain of the satellite n, respectively. Multiplication of both quantities represents the equivalent isotropic radiated power. The quantity λ is the signal's wavelength, and R_n is the distance between the nth satellite and the ground unit.

The signal received by the unit (that faces down) on the UAS can be written as

$$\overline{CN}^{F}_{0,n} = K_n R_s(\theta_{i,n}, \phi_{i,n}) \overline{G}_R(\theta_{i,n}, \theta_P) \tag{3}$$

where $\theta_{i,n}$ is the incidence angle, which is the same as defined in a specular reflection scenario. The phone's relative orientation with respect to the nadir will be modified due to the motion of the UAS, so the impact of the orientation is represented by the UAS pitch angle θ_P in the above formula. The constant K_n is practically the same as the one in (1) since the transmitter is in the medium earth orbit (MEO), which is far away ($\sim$ 20 000 km) from both receivers. Finally, $R_s(\theta_{i,n}, \phi_{i,n})$ is the reflectivity, which is the parameter of interest to be estimated for various land remote sensing purposes. It carries useful information around the specular point. For row-structured agricultural fields, the azimuth angle of observation can be important, so $\phi_{i,n}$ represents the azimuth angle of the given satellite n to indicate such dependence.

Taking the ratio of simultaneous measurements of direct and reflected signals (or logarithmic difference) leads to the cancellation of the common factor K_n for each satellite, but a residual factor will remain due to misalignment of the UAS unit from the nadir direction as shown below

$$\mathrm{Ratio}_n = \frac{\overline{CN}^{F}_{0,n}}{\overline{CN}^{G}_{0,n}} = \mathrm{R}_s\left(\theta_{i,n}, \phi_{i,n}\right) \Delta\overline{\mathrm{G}}_R\left(\theta_{i,n}, \theta_p\right) \tag{4}$$

where the offset factor is given by

$$\Delta\overline{\mathrm{G}}_R\left(\theta_{i,n}, \theta_p\right) = \frac{\overline{\mathrm{G}}_R\left(\theta_{i,n}, \theta_p\right)}{\overline{\mathrm{G}}_R\left(\theta_{i,n}\right)}. \tag{5}$$

For a straight flight in stable weather, such offset is expected to remain constant and can be estimated using reflections over known surfaces such as water bodies. This is further explored in the following sections.

B. Challenges

We outline a list of challenges regarding the impact of the irregular antenna on the ground and UAS measurements.

1) Ground Unit: The smartphone's GNSS antenna has been designed for navigation and positioning purposes, where irregularities in the radiation pattern do not significantly affect positioning accuracy. However, these irregularities in the radiation

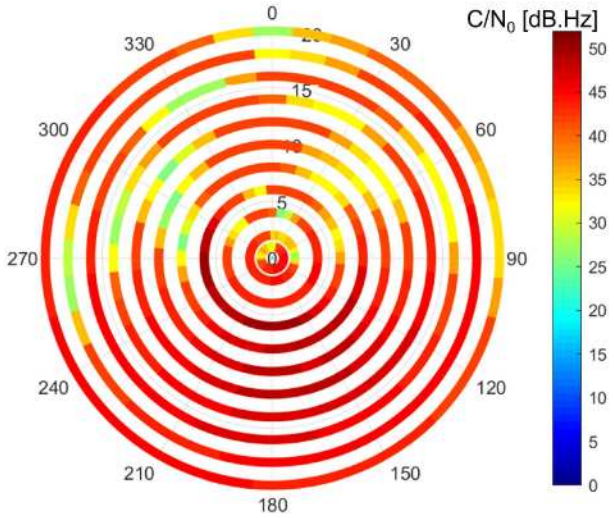

Fig. 2. GNSS signal fluctuation due to smartphone's irregular antenna radiation pattern, measured with pan-tilt mechanism.

pattern can affect remote sensing measurements, as changes in smartphone orientation can perturb the received signal. A pan and tilt mechanism was designed to test the angular and orientation dependencies of the GNSS signal on the smartphone [30] and [31]. It was observed that the inbuilt antenna inside the smartphone is highly angle-dependent, as an example cycle is depicted in Fig. 2, where each ring represents a tilt angle ranging from 0 to 20° with a 2° interval for all 360° azimuth angles. The change of color in each ring represents the change of CN_0 power within one 360° rotation of the smartphone in 36 s. The smartphone's inbuilt GNSS chip and antenna performance have been tested with a series of experiments in [30]. For the fixed or nonspinning receiver on the ground, the GNSS signal strength is a strong function of the satellite's azimuth angle, elevation angle, and receiver orientation.

2) UAS Unit: The receiver experiences more angular movement compared to the ground receiver. As the UAS follows a predetermined flight path with a constant speed, the pitch, roll, and course angles can change depending on the flight direction and velocity of the wind. A typical UAS flight path and corresponding flight dynamics for this study are given in Fig. 3(a) and (b), respectively. When the UAS flies towards the South, the UAS upper side inclines towards the South, and the bottom side inclines towards the North. As a result, the downward-looking antenna's bore-sight radiation pattern displaces North from its normal. In contrast, when the UAS flies towards the North, the UAS upper side inclines towards the North, and the bottom side inclines towards the South. As a result, the downward-looking antenna's boresight radiation pattern displaces towards the South from its normal. The effect of the UAS's pitch angle on the receiver attached underneath is illustrated in Fig. 4. The pitch angle of the UAS introduces a residual angle for the South flight lines and North flight lines. The signals received by the nonspinning UAS platform are, on the other hand, expected to be a strong function of the satellite's azimuth angle, elevation angle, and pitch angle of the UAS.

C. Proposed Solution

The smartphone's built-in GNSS antenna's irregular radiation pattern degrades the GNSS signal quality. A spinning receiver system has been designed to correct these irregularities by physically averaging the received signals on the ground and UAS-based receiver platform. The receiver accumulates GNSS signals while spinning at a constant r/min in its azimuth direction. A detailed spinning experiment with various rotation speeds (i.e., 30, 60, 90, and 120 r/min) has been performed, and found that the speed of 60 r/min is an optimum choice to smooth out the smartphone's antenna radiation pattern irregularities, as discussed next section. The 60 r/min corresponds to one full rotation in one second; thus, the smartphone's GNSS receiver samples a 1 Hz continuous signal over 360° equally during each rotation, leading to one full rotation of the antenna pattern for each C/N_0 output.

For the flight experiment (the concept implementation), one upward-facing spinning smartphone has been placed on the ground in an unobstructed open sky area that receives direct signals while another down-facing spinning smartphone is mounted underneath a UAS to receive the ground-reflected GNSS signals. Both units are designed to rotate at a constant and same speed (e.g., 60 r/min). As we argued previously, such rotation is expected to reduce or lessen the impact of the antenna on the measurements. Since the ground unit is looking straight up while the drone unit can be slightly off the nadir due to the pitch of the drone, in fact, such pitch angles will be different depending on whether it is flying North or South direction. As a result, one needs to consider different residual factors for any direction (e.g., North or South). The residual is expected to be a smooth function of each GNSS satellite's elevation angle and the UAS's pitch angle due to the pattern averaging in azimuth.

III. Experiments

A. Instruments and Hardware Preparation

The spinning ground platform is designed with a high torque 12 V stepper motor. The speed of the motor is controlled using a programmable motor controller to maintain constant r/min. The ground smartphone GNSS receiver is placed on an 18-inch (45.72 cm) aluminum mesh plate to isolate any interference signal from the motor and other electronics from the rotating mechanism platform. The ground mesh plate is attached to the top of the motor using a custom-made adapter. Fig. 5 displays the spinning and stationary receiver placed in an open sky area.

For the UAS-based receiver, the UAS is custom-built on a carbon fiber-based quad-copter frame. An open-source flight control software named mission-planner and the open-source Pixhawk flight controller has been used to build the UAS platform. The spinning platform is attached underneath the UAS as a payload using a dampening adapter to cancel out excessive vibration to the receiver. The down-facing rotating mechanism on the UAS platform uses the same instrument as the ground spinning system to avoid any discrepancies between the two receiver systems. The 18-inch diameter (45.72 cm) aluminum plate is made of meshes whose size is smaller than 0.635 cm.

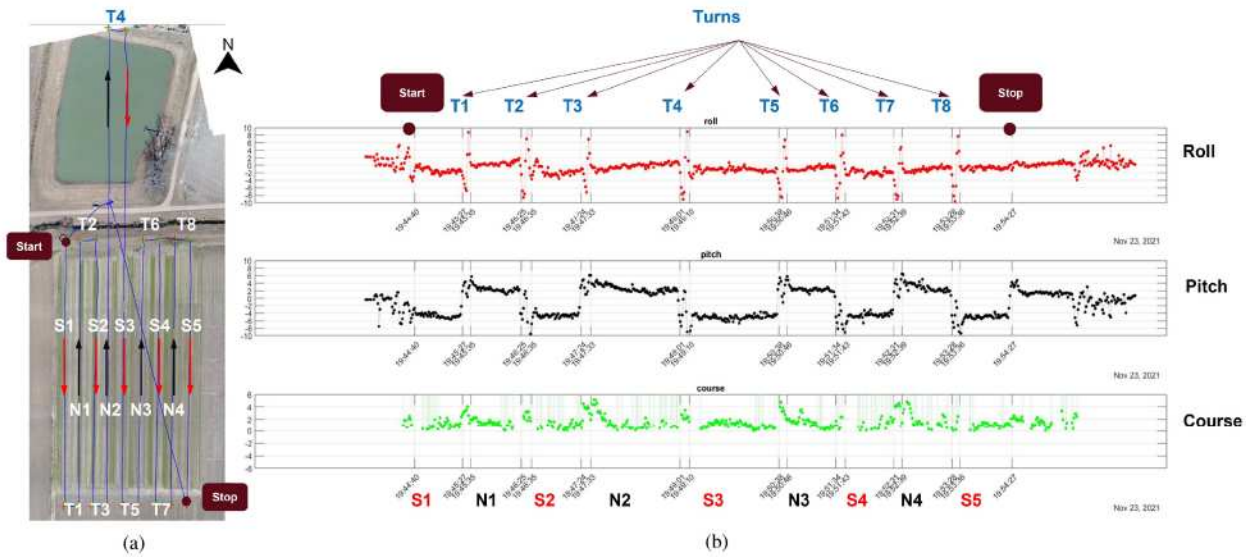

Fig. 3. (a) UAS flight path in the experiment field labeled with turns and flight direction (b) UAS flight dynamics represents the change of roll, pitch, and course during the flight. The flight path consists of nine straight flight lines (i.e., four North (N) and five South (S)) directions with eight turns (T). The UAS heading is kept fixed.

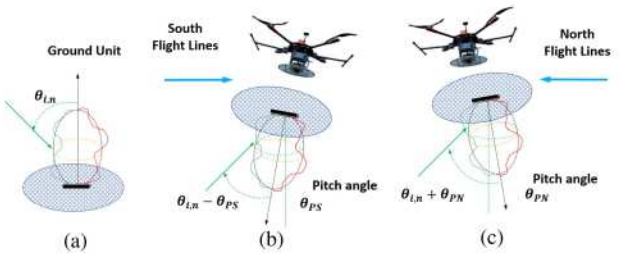

Fig. 4. (a) Upward-looking spinning ground receiver. UAS equipped with a spinning receiver flying towards (b) South and (c) North, showing the effect of pitch angle on the receiver antenna radiation pattern.

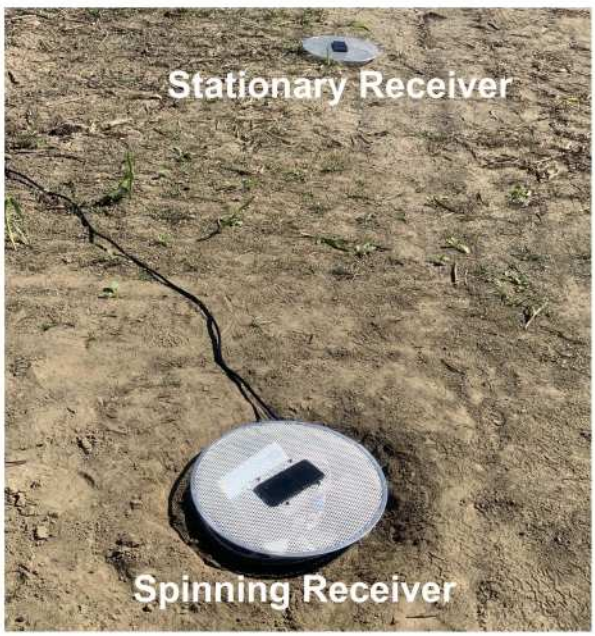

Fig. 5. Ground spinning and stationary receiver collecting a direct line of sight GNSS signals over the course of four hours.

The gaps are less than $1/10$th of the wavelength of L1 frequency band, which effectively obstructs the direct line-of-sight signals from GNSS satellites; at the same time, the mesh structure lets the air flow within the mesh easily. A down-facing GoPro camera is attached underneath the UAS for visual referencing. Fig. 1(b) displays the fully configured UAS platform with the rotating unit.

B. Description of the Study Field

The study has been conducted in a 210 m by 110 m (2.31 ha) field (lower left corner 33°28′15.70″N : 88°46′27.53″W) at the R. R. Foil Plant Science Research Center, Mississippi State University, Starkville, MS, USA in October and November 2021. The average temperature of the study area is 17.8° Celsius over the year. In the study area, July experiences the highest average monthly temperature; in January, it becomes the lowest. The average annual precipitation is approximately 1329 mm. The humidity varies within a range from 55% to 66% monthly. The field is located at 92 m above sea level. The field was barren during the time of the study. However, the row structure in the field was spaced 38 inches (96.5 cm). The North side of the study field consists of a large water body and a small creek, as shown in Fig. 3(a).

C. Experiment Setup and Data Collection

Fig. 6 provides an experiment matrix that describes several experiment setups and patterns we have performed. The ground and UAS section of the table defines the smartphone receiver placed on the ground and UAS platform, respectively. For the spinning test experiment, one upward-facing spinning smartphone and an identical nonspinning smartphone are placed on the ground in an unobstructed open sky area. Each day, the phones were run over a period of approximately four hours with various configurations (i.e., four different directions for

Date	Ground		UAS			
	Stationary	Spining	Spining			
	Phone A	Phone B	Phone A	Phone A	Phone A	Phone A
	Direction	Speed	Flight #1	Flight #2	Flight #3	Flight #4
24-Oct	North	30 rpm				
26-Oct	West	60 rpm				
27-Oct	South	90 rpm				
1-Nov	East	120 rpm				
23-Nov		60 rpm	60 rpm	60 rpm	60 rpm	60 rpm
27-Nov		60 rpm	60 rpm	60 rpm	60 rpm	60 rpm
28-Nov		60 rpm	60 rpm	60 rpm	60 rpm	60 rpm

Fig. 6. Experiments matrix for ground spinning and stationary smartphone GNSS receiver to investigate the direct line of sight GNSS signals and UAS-base spinning smartphone flights for surface reflectivity analysis. (The two smartphones used in this experiment are named Phone A and Phone B).

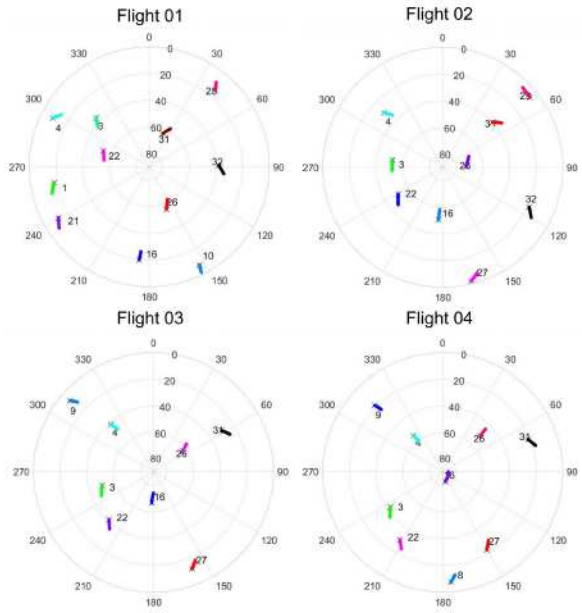

Fig. 7. Sky plot of the GNSS satellites trajectory during four flight experiments over the course of the day. The numbers inside the plot represent the satellites' PRN numbers.

the stationary phone and four different rotation speeds for the spinning phone) on four different days. The start time of these measurements shifted accordingly as the same satellite configuration is repeated four min earlier every day for one and the same location due to the sidereal revolution period of the GPS satellites (11 h 58 min). The open sky receivers continuously collect GNSS signals from all available satellites above the horizon. The duty cycle has been selected to 100% and recorded 1 Hz continuous signal for the whole experiment period. For the flight test, another identical spinning smartphone with 60 r/min, as in the ground spinning smartphone, was attached. The duty cycle of the UAS-based receiver is also selected to 100% and receives a 1 Hz continuous signal. A total of four flights were conducted during each data collection day, with an interval of at least one hour between each flight, over the course of three days. Similar to the spinning test, the start time of the flight days shifted accordingly to match the GPS satellites' positions each day.

The UAS flies to a predetermined flight path while accumulating reflected GNSS signals. The data is received and recorded on the smartphone. The UAS flight speed is an important flight setting to select during the data collection. The faster the flight speed is, the faster it covers the same area but decreases the ground resolution as it travels longer distances during the integration time. In contrast, the slower the speed is, the finer the footprint is, but a larger battery capacity is needed to cover the full study area and it will take longer to cover the same area. In this study, 5 m/s flight speed at a 15 m altitude has been selected as optimal in terms of coverage and ground resolution. The smartphone GNSS receiver integrates the received signal every second that corresponds to an area of 5 m long footprint (its width depends on the receiver/satellite geometry) on the ground from each satellite. The GNSS constellations operate from medium earth orbit (MEO) at an altitude of approximately 20 000 km. The distance between the ground receiver and the UAS receiver smartphone was 15 m. Given the altitude of the GNSS constellation, we assumed that the signal strength changes due to the height difference between the two smartphones were negligible. The onboard flight controller records the flight dynamics of the UAS, which includes the latitude, longitude, roll, pitch, yaw, altitude, and other navigation parameters for the full flight path. The UAS flight data and the GNSS receiver's data are UTC (Coordinated Universal Time) time synchronized for the correlation of the received data and the UAS geospatial position. The flight path consists of nine straight flight lines (i.e., four North (N) and five South (S)) directions with eight turns (T). The UAS heading is kept fixed (varied from 0° to 2° along straight flight lines). South flights had a pitch angle of 3°, while North flights had a pitch angle of −5° during the experiment. The variations in both cases were less than 1° for each line. The roll angle stayed relatively constant for each straight line but varied slightly from line to line. A sample of UAS flight dynamics is shown in Fig. 3(b).

Fig. 7 shows the GNSS satellites' position in a sky plot during the experiment time on 23 November and four data collection flights, where the numbers around the outermost circle represent the azimuth angle (0° to 360°) and the smaller circles represents the elevation angle. The innermost point is the 90° elevation angle and decreases to 0° elevation angle at the horizon.

D. Data Format and Data Preparation for Analysis

The GNSS data is recorded in a Receiver Independent Exchange (RINEX) 3.03 format using a Google Play-Store APP, "RINEX ON". The "RINEX ON" APP receives and record GNSS data for all the available GNSS constellations above the horizon. The APP is freely available for all to download from Google Play-Store. The RINEX data is decoded and arranged into a readable format for both ground and UAS receivers. The individual GNSS satellites' azimuth, elevation, and C/N_0 data are extracted and arranged according to the time-synchronized geospatial location of the UAS using the latitude and longitude of the UAS for each second. The C/N_0 data is then processed to estimate the reflectivity of the studied field.

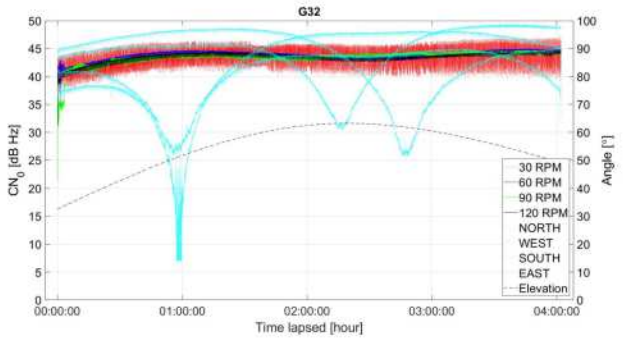

Fig. 8. Sample ground test result from time-series experiments on four different days (October 24, 26, 27, and November 1).

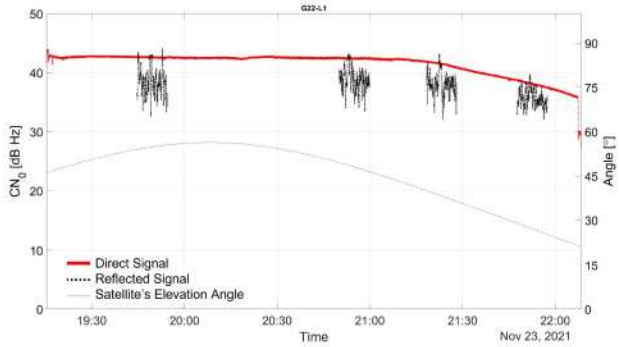

Fig. 9. Sample flight test result from the experiment that took place on November 23.

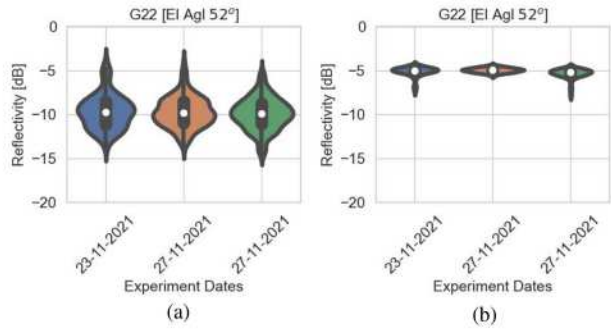

Fig. 10. Violin plot of the reflectivity: (a) Distribution of reflectivity from the field region, (b) Distribution of reflectivity from the water body during flight experiments of three different days.

IV. Results

We first investigate the impact of the rotation speed on the received signal strength for roughly a 4-hour time period. Second, we compare the results from measurements with the phone on a small UAS and the ground. We then compare the bound of the reflectivity estimates against theoretical calculations.

A. Ground Spin Test

Fig. 8 shows the received signal strength (C/N_0) for stationary and spinning phones in an unobstructed open sky area. The cyan color represents phones that are oriented towards North, East, South, or West in each day. As clearly seen, the received signal has dips at different levels and locations for each orientation. One would expect such dips to appear if we orient the phone in different directions. This result is expected and is the main reason for spinning the phone with the ground plate. The other colors represent the signal strengths from different rotation speeds (i.e., 30, 60, 90, and 120 r/min). As seen from the same plot, the dips disappear for each rotation, but the 30 r/min rotation fluctuates more than the other rotations as it samples the data over half a cycle only. The other rotation choices have similar signal levels and variations. While we show the results from GPS L1 Pseudorandom Noise (PRN) Code # 32, we also obtained similar results for other GNSS satellites. This experiment's major implication was that we successfully removed the dips of the antenna radiation by rotating the phone at more than 60 r/min (i.e., at least one full rotation every second). It is worth noting that the utilization of multiples of 60 r/min, such as 120 r/min, was observed to produce results that were similarly effective in smoothing signal fluctuations as the 60 r/min configuration. However, due to the compatibility of the 60 r/min setting with the 1 Hz data acquisition frequency and the increased vibration introduced to the UAS structure during flight, and the higher power consumption associated with higher r/min settings, this particular configuration was ultimately chosen for implementation in both the ground and UAS platforms.

B. Flight Spin Test

Next, we fixed the speed of rotation for both flight and ground units at 60 r/min. During a typical flight, the smartphone's GNSS receiver collects data from approximately five GPS satellites, with the elevation angle below 30° and above 65° being masked. In this analysis, the results from the flight experiment for GPS L1 PRN # 22 are given in Fig. 9 while we obtain similar results for other satellites (not shown here). The black colors denote the data collected by the down-facing unit on the UAS, while the red color represents the data collected upward-facing ground unit. The dashed lines denote elevation angles. As expected, the signal strength from the ground unit (that collects the direct signal) does not have dips. It exhibits a uniform response during the experiment duration, about four hours. The received signals by the drone units (collects reflected signal) fluctuate since the specular points travel over different land features as the drone flies along a straight path. As we hypothesized, the reflected signal is lower than the direct signal, so the signal ratio in (4) represents a proxy for the reflectivity. However, the reflected signal is occasionally larger than the direct signal. These instances happen when the drone turns from one flight line to another one. Additionally, as the drone flies, the phone is not pointing straight down to the ground due to the pitch angle of the drone. This indicates that the angular dependence of the antenna pattern still needs to be compensated.

Fig. 10 shows the distribution of reflectivity (after the offset adjustment of 5 dB) over the field and water body as violin plots during the first flights of three different days. The violin plot depicts summary statistics and the density of each measurement. The offset value is determined based on the water surface

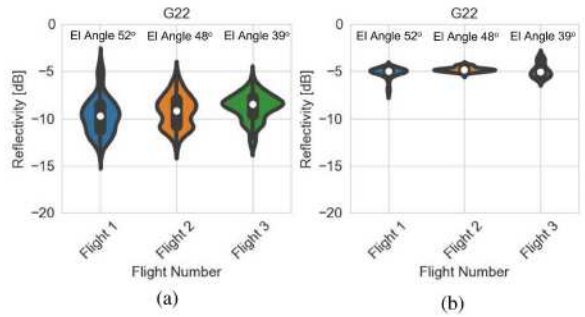

Fig. 11. Violin plot of the reflectivity: (a) The distribution of reflectivity from the field region, (b) the distribution of reflectivity from the water body, during three flight experiments over the course of a single day (November 23), with a varying elevation angle of satellite G22.

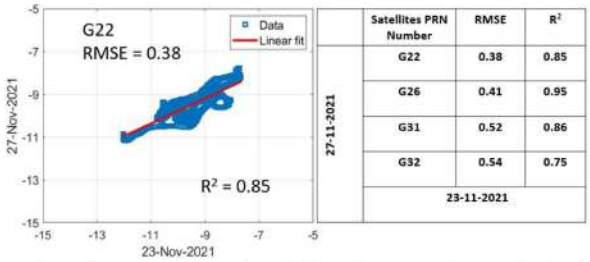

Satellites PRN Number	RMSE	R^2
G22	0.38	0.85
G26	0.41	0.95
G31	0.52	0.86
G32	0.54	0.75
23-11-2021		

Satellites PRN Number	RMSE	R^2
G22	0.66	0.80
G26	0.36	0.96
G31	0.39	0.95
G32	0.43	0.66
23-11-2021		

Satellites PRN Number	RMSE	R^2
G22	0.70	0.78
G26	0.50	0.92
G31	0.61	0.88
G32	0.46	0.56
27-11-2021		

Fig. 12. Reflectivity correlation between multiple satellites from each of the first flights of three experiment days.

reflectivity. As mentioned previously, the start time of the flight days shifted accordingly to match the GPS satellites' positions each day. Similarly, every second, third, and fourth flight is also synchronized UTC time. The average reflectivity over water is higher than the average reflectivity over land. The variations over water are much smaller than the variations over land, as expected. The aforementioned observations and the reflectivity distributions remained similar over multiple days, where the field conditions did not change in three days (no rain between flights). There are some instances where the land reflectivity goes over the water reflectivity, but these can be considered outliers and do not represent the general trend.

Fig. 11 shows the distribution of reflectivity over the field and water body for three flights on the same day (i.e., November 23). Since these flights happened at different times, the satellite elevation angles of these observations are different. The fourth flight is excluded from the reflectivity analysis due to the elevation angle of below 30°. This result shows a minor dependence of the water reflectivity on the elevation angle, but such dependence has somewhat more for the reflectivity over land without a particular trend. The nominal polarization of the inbuilt antenna is linearly polarized, but it is being rotated every second, so the polarization nature of the reflectivity still remains to be further explored in order to arrive intuitive trend for the angular behavior of the reflectivity.

Fig. 12 represents the correlation of overall reflectivity from the field and water body for multiple satellites and different days. The data and the regression line shows the reflectivity correlation between the first flight experiment of November 23 and 27. The rest of the satellites' reflectivity correlation between the three experiment days is represented in tabular format. These results indicate that the methodology shows a repeatable trend across satellites and different days as long as the drone satellite geometry remains the same.

C. Estimated Reflectivity Bound

In this section, we will argue if the distribution of reflectivities over the land is within the theoretical calculations. In Fig. 13, the geospatial (a) and temporal (b) plots of reflected signals are given in the upper panel, while the bottom panel shows the same plots in (c) and (d) for reflectivity estimates. The spatial distribution of the reflections over water and land shows the clear distinction between the water and the land. The variation over land is larger while it is stable over water, as consistent with the previous discussion. However, the direct comparison of point-by-point moisture level estimation was not possible as it requires many soil moisture probes available on the field. Instead, the Fresnel reflectivity of linear polarized signals with flat (dashed lines) and smooth rough surface of rms height of 1 cm (solid lines) are calculated for water, wet soil (0.40 m^3 m^{-3}), and dry soil (0.05 m^3 m^{-3}) for expected extreme cases. The values are added as the bounds in the temporal reflectivity plot in Fig. 13(d). The result indicates that estimated values are within the theoretical limits. While the experiment was performed on a barren field, the effect of vegetation can add another dimension for such comparison for crop fields.

V. Discussion

The GNSS chips have become cheaper, smaller, and more powerful. Now, they are ubiquitous and available virtually in every mass-market smartphone. In addition, there are now mobile devices on the market capable of recording raw GNSS measurements. Direct access to raw GNSS data from mass-market devices running the Android Nougat (or newer) operating system [34], has opened up new solutions in navigation [35] and remote sensing [36]. For instance, several groups investigated the use of Android devices to perform GNSS- Interferometry to measure sea level [35] or effective reflector heights [37], [38]. In addition to the altimeter applications, a few initial studies [29], [31] has also utilized smartphones for precision agriculture. This section will discuss some of the tradeoffs involved in the present study.

A fully customized UAS has been developed for this study as it provides enough flight time to cover the $\sim$ 2.31 ha study field while carrying the spinning instruments and smartphone as payload. Spinning speed of 60 r/min has been empirically selected for the study by carefully testing different (30, 60, 90, and 120 r/min) speed combination. A 24 V LiPo battery was used to spin the smartphone. At 30, 60, 90, and 120 r/min, the power consumption was 8 W, 12 W, 18 W, and 24 W, respectively. A

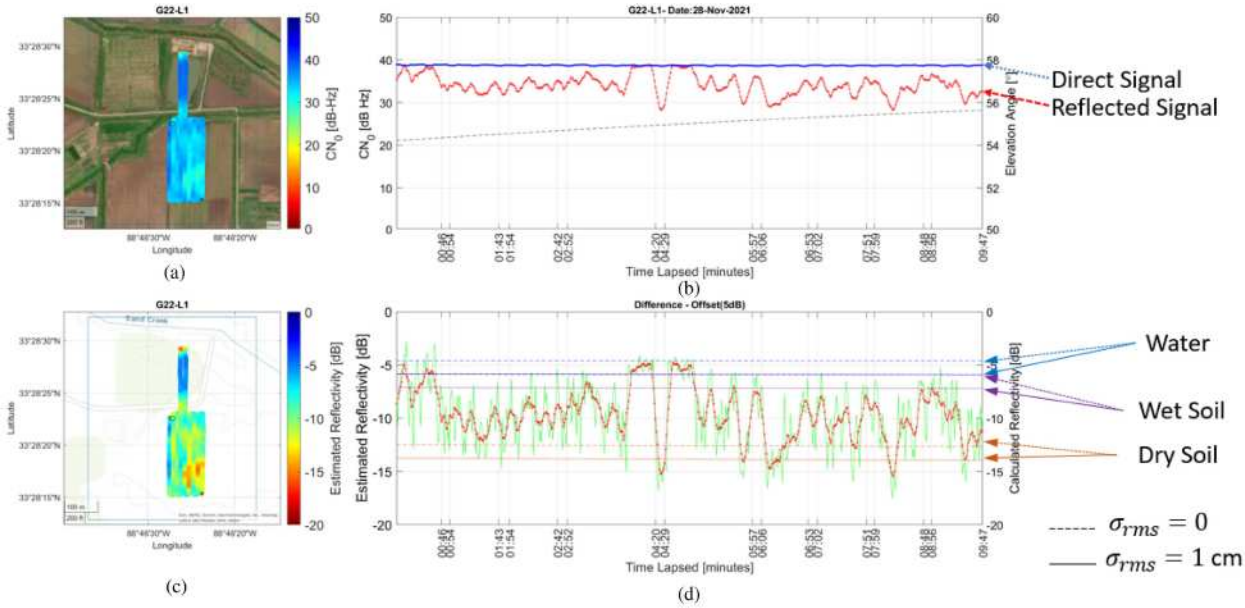

Fig. 13. (a) Geospatial plot of reflected signal in dB-Hz, (b) comparison of direct and reflected signals in time series, (c) geospatial plot of reflectivity, (d) temporal plot of reflectivity with theoretical bounds for flat, smooth surfaces of water, wet soil, and dry soil.

separate LiPo battery was used to power the spinning system on the UAS platform. The UAS flight battery and flight control system were independent of the spinning system. A spinning rate of 60 r/min was found to provide sufficient smoothing of the reference and ground-reflected signal to estimate the reflectivity accurately. This setting also matches the 1 Hz signal acquisition rate. Although a spinning rate of 120 r/min performs similarly well, the 60 r/min setting was selected for this study due to the reduced vibration introduced to the UAS structure during flight and the lower power consumption associated with lower spinning rates.

The smartphone (Xiaomi Mi-8) used in our experiment has a linear polarized antenna [39]. When RHCP GNSS signals reflect from the ground surface, their polarization changes to left-hand circularly polarized (LHCP) signals. The smartphone underneath the UAS platform receives these LHCP signals with its linearly polazired antenna with 3 dB less power than it would receive a LHCP signal with an LHCP antenna. However, as we calculate the surface reflectivity by taking the logarithmic difference between the ground-reflected signal and the direct or reference signal, the 3 dB loss in the received signal does not affect the reflectivity calculation.

The satellite's elevation angle has some effect on the signal power. We empirically observed that satellites with elevation angles below 30° and above 65° do not provide consistent signal strength. The lower elevation angle (below 30°) satellite's signal experiences more multipath and becomes weaker, and at the higher elevation angles (above 65°) becomes stronger due to the boresight radiation pattern of the GNSS antenna in the smartphone. Because of this effect, we excluded the satellites' signal with elevation angles below 30° and above 65° from our analysis.

The offset that we calculated in the present analysis is to compensate for the antenna effect due to the pitch of the UAS. It was estimated empirically by matching the reflectivity of the water to the measured signal strength difference. The water reflectivity is used as a reference. The water body we used in our analysis was moderately calm so this offset can be used in similar situations. However, if the water waves are too rough due to the wind, the reflectivity of the water and the UAS dynamics will change, and a new offset will need to be calculated. We corrected the UAS pitch angle effect on the smartphone's antenna radiation pattern for North and South direction flight lines separately.

In this article, we focused on estimating surface reflectivity accurately using a smartphone. However, surface reflectivity depends on several factors, such as surface soil moisture, surface roughness, vegetation types, vegetation height, and vegetation density. These factors can introduce errors when retrieving surface soil moisture from the reflectivity measurements unless these effects are characterized accurately. In addition, a direct comparison of point-by-point moisture level estimation was not possible in this study, which would require a large number of soil moisture probes available in the field. One could use a rover equipped with soil moisture probes to collect soil moisture data from the study field while collecting the reflectivity data using the UAS-based system. In our future work, we will focus on soil moisture retrieval from bare and vegetated soil using surface reflectivity while considering the effects of these factors.

One might expect that someone will not put their daily used smartphone on a UAS to measure soil moisture. However, we can consider the smartphone to be a standalone GNSS receiver, not an everyday-use personal mobile communication device. An off-the-shelf GNSS receiver consists of at least two parts (GNSS receiver unit and receiving antenna) and requires specific knowledge to operate the system. On the other hand, a smartphone has its own built-in GNSS chip and GNSS antenna. One can use a spare smartphone and an app to receive and

record the GNSS signal without having any prior knowledge about GNSS receiver systems. Moreover, smartphones are more ubiquitous than an off-the-shelf GNSS receiver, which allows more access to general public, especially farmers in economically distressed areas and developing countries, to observe their agricultural land. Apart from the soil moisture measurement, this technique can be applied for other remote sensing problems such as monitoring wetlands, snow, and floods.

VI. Conclusion

Our previous study indicated that the main limitation of GNSS-R from smartphones was the irregular antenna pattern of smartphones. In this article, we proposed a novel approach to lessen the impact of the antenna on the received signal by spinning the smartphone on a rotating ground plate, which requires no explicit knowledge of antenna pattern characteristics. We conducted several experiments to demonstrate the feasibility of such an approach. The results indicated that spinning the phones at more than 60 r/min eliminates the dips in the radiation pattern and makes it quite uniform. We estimated surface reflectivity and compared it with theoretical calculations and possible bounds. The unique features of this work can be summarized as follows.

1) This study implements a ubiquitous GNSS-R approach using a smartphone mounted on a small UAS platform in conjunction with another smartphone on the ground to estimate the surface reflectivity.
2) Smartphones' irregular antenna radiation pattern has been identified and corrected by developing a spinning mechanism.
3) The reflectivity is estimated by taking the logarithmic difference between two simultaneous measurements of ground and UAS units, both of which use the same smartphone and spinning mechanisms.
4) A low-cost meshed plate has been used to isolate the direct and reflected signals on the UAS platform since the UAS's low altitude operation (15 m) prevents isolating direct and reflected signals in time, as is done by the spaceborne GNSS-R receivers.
5) The bound of estimated soil reflectivity due to surface geophysical variations (i.e., dry to wet soil with smooth surface) has been estimated, and the level has been adjusted with respect to the reflectivity over the water body.

The future work will include determining the offset value and quantitative validation of the results with land features.

References

[1] C. M. K. Gardner, D. Robinson, K. Blyth, and J. David Cooper, "Soil water content," in *Soil and Environmental Analysis*. Boca Raton, FL, USA: CRC Press, 2000, pp. 13–76.

[2] U. Shafi, R. Mumtaz, J. García-Nieto, S. A. Hassan, S. A. Zaidi, and N. Iqbal, "Precision agriculture techniques and practices: From considerations to applications," *Sensors*, vol. 19, no. 17, 2019, Art. no. 3796.

[3] B. F. Schwartz, M. E. Schreiber, and T. Yan, "Quantifying field-scale soil moisture using electrical resistivity imaging," *J. Hydrol.*, vol. 362, no. 3/4, pp. 234–246, 2008.

[4] R. Tsheko and M. J. Savage, "Calibration of a frequency-domain reflectometer for determining soil-water content in a clay loam soil," *Water Sa*, vol. 32, no. 1, pp. 37–42, 2006.

[5] E. Veldkamp and J. J. O'Brien, "Calibration of a frequency domain reflectometry sensor for humid tropical soils of volcanic origin," *Soil Sci. Soc. Amer. J.*, vol. 64, no. 5, pp. 1549–1553, 2000.

[6] J. Xu, X. Ma, S. D. Logsdon, and R. Horton, "Short, multineedle frequency domain reflectometry sensor suitable for measuring soil water content," *Soil Sci. Soc. Amer. J.*, vol. 76, no. 6, pp. 1929–1937, 2012.

[7] J. Kodikara, P. Rajeev, D. Chan, and C. Gallage, "Soil moisture monitoring at the field scale using neutron probe," *Can. Geotech. J.*, vol. 51, no. 3, pp. 332–345, 2014.

[8] A. D. Coelho, B. G. Dias, W. de Oliveira Assis, F. de Almeida Martins, and R. Cassares Pires, "Monitoring of soil moisture and atmospheric sensors with Internet of Things (IoT) applied in precision agriculture," in *Proc. 14th Technol. Appl. Electron. Teach. Conf.*, 2020, pp. 1–8.

[9] T. Syrovy et al., "Fully printed disposable IoT soil moisture sensors for precision agriculture," *Chemosensors*, vol. 8, no. 4, 2020, Art. no. 125.

[10] M. Leone et al., "Fiber optic soil water content sensor for precision farming," *Opt. Laser Technol.*, vol. 149, 2022, Art. no. 107816.

[11] J. Lloret, S. Sendra, L. Garcia, and J. M. Jimenez, "A wireless sensor network deployment for soil moisture monitoring in precision agriculture," *Sensors*, vol. 21, no. 21, 2021, Art. no. 7243.

[12] K. M. Larson, E. E. Small, E. D. Gutmann, A. L. Bilich, J. J. Braun, and V. U. Zavorotny, "Use of GPS receivers as a soil moisture network for water cycle studies," *Geophys. Res. Lett.*, vol. 35, no. 24, 2008, pp. 1–5.

[13] K. M. Larson, E. E. Small, E. Gutmann, A. Bilich, P. Axelrad, and J. Braun, "Using GPS multipath to measure soil moisture fluctuations: Initial results," *GPS Solutions*, vol. 12, no. 3, pp. 173–177, 2008.

[14] K. Yu, *Theory and Practice of GNSS Reflectometry*. Berlin, Germany: Springer, 2021.

[15] K. Yu, C. Rizos, D. Burrage, A. G. Dempster, K. Zhang, and M. Markgraf, "An overview of GNSS remote sensing," *EURASIP J. Adv. Signal Process.*, vol. 2014, no. 1, pp. 1–14, 2014.

[16] V. U. Zavorotny, S. Gleason, E. Cardellach, and A. Camps, "Tutorial on remote sensing using GNSS bistatic radar of opportunity," *IEEE Geosci. Remote Sens. Mag.*, vol. 2, no. 4, pp. 8–45, Dec. 2014.

[17] C. Ruf et al., "CYGNSS: Enabling the future of hurricane prediction [remote sensing satellites]," *IEEE Geosci. Remote Sens. Mag.*, vol. 1, no. 2, pp. 52–67, Jun. 2013.

[18] M. M. Nabi, V. Senyurek, A. C. Gurbuz, and M. Kurum, "Deep learning-based soil moisture retrieval in CONUS using CYGNSS delay–Doppler maps," *IEEE J. Sel. Topics Appl. Earth Observ. Remote Sens.*, vol. 15, pp. 6867–6881, 2022.

[19] D. Entekhabi et al., "The soil moisture active passive (SMAP) mission," *Proc. IEEE*, vol. 98, no. 5, pp. 704–716, May 2010.

[20] Y. H. Kerr, P. Waldteufel, J-P Wigneron, J. Martinuzzi, J. Font, and M. Berger, "Soil moisture retrieval from space: The soil moisture and ocean salinity (SMOS) mission," *IEEE Trans. Geosci. Remote Sens.*, vol. 39, no. 8, pp. 1729–1735, Aug. 2001.

[21] M. Kurum et al., "A UAS-based RF testbed for water utilization in agroecosystems," in *Proc. Auton. Air Ground Sens. Syst. Agricultural Optim. Phenotyping*, 2021, vol. 11747, pp. 74–88.

[22] M. T. Gamba, G. Marucco, M. Pini, S. Ugazio, E. Falletti, and L. L. Presti, "Prototyping a GNSS-based passive radar for UAVs: An instrument to classify the water content feature of lands," *Sensors*, vol. 15, no. 11, pp. 28287–28313, 2015.

[23] M. T. Gamba, S. Ugazio, G. Marucco, M. Pini, and L. L. Presti, "Light weight GNSS-based passive radar for remote sensing UAV applications," in *Proc. IEEE 1st Int. Forum Res. Technol. Soc. Ind. Leveraging Better Tomorrow*, 2015, pp. 341–348.

[24] R. Imam, M. Pini, G. Marucco, F. Dominici, and F. Dovis, "UAV-based GNSS-R for water detection as a support to flood monitoring operations: A feasibility study," *Appl. Sci.*, vol. 10, no. 1, 2019, Art. no. 210.

[25] R. Imam, M. Pini, G. Marucco, F. Dominici, and F. Dovis, "Data from GNSS-based passive radar to support flood monitoring operations," in *Proc. Int. Conf. Localization GNSS*, 2019, pp. 1–7.

[26] A. Regmi, T. Hänninen, M. E. Leinonen, A. Pärssinen, and M. Berg, "Dynamic dual polarized GNSS reflectometry using UAV," in *Proc. 15th Eur. Conf. Antennas Propag.*, 2021, pp. 1–5.

[27] Y. Jia and P. Savi, "Sensing soil moisture and vegetation using GNSS-R polarimetric measurement," *Adv. Space Res.*, vol. 59, no. 3, pp. 858–869, 2017.

[28] H. Issa, G. Stienne, S. Reboul, M. Raad, and G. Faour, "High-rate GNSS reflectometry for water body detection using low altitude airborne carrier," in *Proc. IEEE Specialist Meeting Reflectometry GNSS Signals Opportunity*, 2021, pp. 9–12.

[29] V. Senyurek, M. M. Farhad, A. C. Gurbuz, M. Kurum, and A. Adeli, "Fusion of reflected GPS signals with multispectral imagery to estimate soil moisture at subfield scale from small UAS platforms," *IEEE J. Sel. Topics Appl. Earth Observ. Remote Sens.*, vol. 15, pp. 6843–6855, 2022.
[30] M. Kurum, A. Gurbuz, and M. M. Farhad, "GNSS reflectometry from smartphones: Testing performance of in-built antennas and GNSS chips," in *Proc. IEEE Int. Geosci. Remote Sens. Symp.*, IEEE, 2020, pp. 6278–6281.
[31] M. Kurum, M. M. Farhad, and A. C. Gurbuz, "Integration of smartphones into small unmanned aircraft systems to sense water in soil by using reflected GPS signals," *IEEE J. Sel. Topics Appl. Earth Observ. Remote Sens.*, vol. 14, pp. 1048–1059, 2021.
[32] M. Kurum, M. M. Farhad, J. Diao, and A. C. Gurbuz, "A ubiquitous GNSS-R approach using spinning smartphone onboard a small UAS," in *Proc. IEEE Int. Geosci. Remote Sens. Symp.*, 2022, pp. 5208–5211.
[33] J. Diao, M. Hedayati, R. U. Tok, and Y. E. Wang, "Mechanical rotating arrays for sidelobe suppression," in *Proc. USA Nat. Committee URSI Nat. Radio Sci. Meeting*, 2019, pp. 1–2.
[34] S. Malkos, "User location takes center stage in new android OS: Google to provide raw GNSS measurements," *GPS World*, vol. 27, no. 7, 2016, Art. no. 36.
[35] E. Realini, S. Caldera, L. Pertusini, and D. Sampietro, "Precise GNSS positioning using smart devices," *Sensors*, vol. 17, no. 10, 2017, Art. no. 2434.
[36] M. Kurum, A. C. Gurbuz, C. Nelson, L. Orsini, and M. Scheider, "On the feasibility of smartphone-based interferometric GNSS reflectometry," in *Proc. ION Pacific PNT Meeting*, 2019, pp. 635–640.
[37] C. Altuntas and N. Tunalioglu, "Feasibility of retrieving effective reflector height using GNSS-IR from a single-frequency android smartphone SNR data," *Digit. Signal Process.*, vol. 112, 2021, Art. no. 103011.
[38] Z. Liu, L. Du, P. Zhou, Z. Liu, Z. Zhang, and Z. Xu, "Performance assessment of GNSS-IR altimetry using signal-to-noise ratio data from a Huawei P30 smartphone," *GPS Solutions*, vol. 26, no. 2, 2022, Art. no. 42.
[39] L. Guo, F. Wang, J. Sang, X. Lin, X. Gong, and W. Zhang, "Characteristics analysis of raw multi-GNSS measurement from Xiaomi MI 8 and positioning performance improvement with l5/e5 frequency in an urban environment," *Remote Sens.*, vol. 12, no. 4, 2020, Art. no. 744.

Md Mehedi Farhad (Student Member, IEEE) received the B.Sc. degree in electrical and electronic engineering from the Ahsanullah University of Science and Technology, Dhaka, Bangladesh, in 2012. He is currently working toward the Ph.D. degree in electrical and computer engineering with Mississippi State University, Mississippi State, MS, USA.

His research interests include UAS-based GNSS-R techniques, L-band microwave radiometer, and UGV-based GNSS Transmissometry (GNSS-T) techniques for the remote sensing of earth surface geophysical parameters using low-cost and smart devices.

Mehmet Kurum (Senior Member, IEEE) received the B.S. degree in electrical and electronics engineering from Bogazici University, Istanbul, Turkey, in 2003, and the M.S. and Ph.D. degrees in electrical engineering from George Washington University, Washington, DC, USA, in 2005 and 2009, respectively.

He held a Postdoctoral position with the Hydrological Sciences Laboratory, NASA Goddard Space Flight Center, Greenbelt, MD, USA. He is currently an Associate Professor and Paul B. Jacob endowed chair in Electrical and Computer Engineering with Mississippi State University, Mississippi State, MS, USA, where he is also co-Director of Information Processing and Sensing (IMPRESS) Laboratory. His current research interests include recycling the radio spectrum to address the challenges of decreasing radio spectrum space for science while exploring entirely new microwave regions for land remote sensing.

Dr. Kurum was a recipient of the Leopold B. Felsen Award for excellence in electromagnetic in 2013, the URSI Young Scientist Award in 2014, and NSF CAREER award in 2022. He is a Senior Member of IEEE Geoscience and Remote Sensing Society (GRSS) and a Member of U.S. National Committee for the International Union of Radio Science (USNC-URSI). He is currently an Associate Editor for IEEE TRANSACTIONS ON GEOSCIENCE AND REMOTE SENSING and *IEEE Journal of Selected Topics in Applied Earth Observations and Remote Sensing* since 2021. From 2014 to 2021, he served as an Early Career Representative for the International URSI Commission F (Wave Propagation and Remote Sensing).

Ali Cafer Gurbuz (Senior Member, IEEE) received the B.S. degree in electrical engineering from Bilkent University, Ankara, Turkey, in 2003, and the M.S. and Ph.D. degrees from the Georgia Institute of Technology, Atlanta, GA, USA, in 2005 and 2008, both in electrical and computer engineering.

He held a Postdoctoral position with the Georgia Institute of Technology, Atlanta, GA, USA, in 2009 where he researched compressive sensing-based computational imaging problems. He held faculty positions with the TOBB University of Economics and Technology, Ankara, Turkey, and the University of Alabama, Tuscaloosa, AL, USA, between 2009 and 2017 where he pursued an active research program on the development of sparse signal representations, compressive sensing theory and applications, radar and sensor array signal processing, and machine learning. He is currently an Assistant Professor with the Department of Electrical and Computer Engineering, Mississippi State University, Mississippi State, MS, USA, where he is co-Director of Information Processing and Sensing (IMPRESS) Laboratory.

Dr. Gurbuz was the recipient of The Best Paper Award for Signal Processing Journal in 2013, the Turkish Academy of Sciences Best Young Scholar Award in Electrical Engineering in 2014, and NSF CAREER Award in 2021. He was an Associate Editor for several journals such as *Digital Signal Processing* and *EURASIP Journal on Advances in Signal Processing and Physical Communications*.